Supplementary Information

Revealing Electronic Signature of Lattice Oxygen Redox in Lithium Ruthenates and Implications for High-Energy Li-ion Battery Material Designs

Yang Yu[a,*], Pinar Karayaylali[b], Stanisław H. Nowak[c], Livia Giordano[b,d], Magali Gauthier[d, †], Wesley Hong[a], Ronghui Kou[e], Qinghao Li[f], John Vinson[g], Thomas Kroll[c], Dimosthenis Sokaras[c, *], Cheng-Jun Sun[e], Nenian Charles[d], Filippo Maglia[h], Roland Jung[h], Yang Shao-Horn[a,b,d,*]

[a] *Department of Materials Science and Engineering, MIT, Cambridge, MA 02139, USA*

[b] *Department of Mechanical Engineering, MIT, Cambridge, MA 02139, USA*

[c] *SLAC National Accelerator Laboratory, Menlo Park, CA, 94025, USA*

[d] *Research Laboratory of Electronics, MIT, Cambridge, MA 02139, USA*

[e] *Advanced Photon Source, Argonne National Laboratory, Argonne, IL 60439, USA*

[f] *Advanced Light Source, Lawrence Berkeley National Laboratory, CA 94720, USA*

[g] *National Institute of Standards and Technology, Gaithersburg, Maryland 20899, USA*

[h] *BMW Group, Petuelring 130, 80788 Munich, Germany*

[†] *Current address: M.G.: LEEL, NIMBE, CEA, CNRS, Université Paris-Saclay, CEA Saclay 91191 Gif-sur-Yvette, France.*

Corresponding Authors

* Yang Yu (yuy@mit.edu)

* Dimosthenis Sokaras (dsokaras@slac.stanford.edu)

* Yang Shao-Horn (shaohorn@mit.edu)

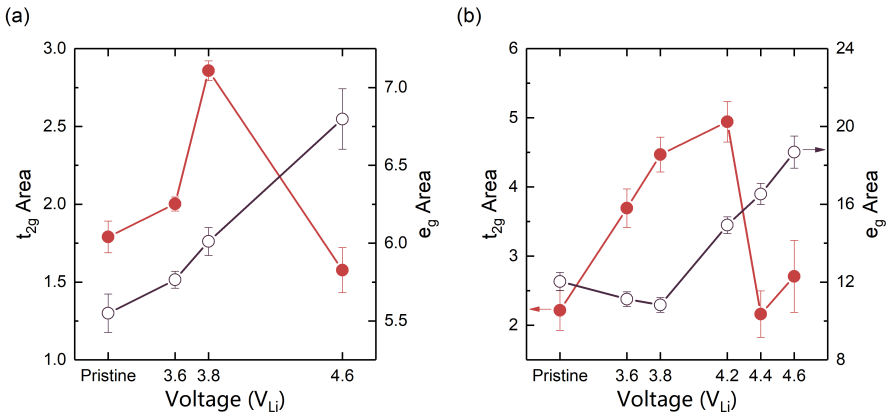

Figure S1: Integrated area underneath t_{2g} (feature a in Figure 1, closed circle) and e_g (feature b in Figure 1, open circle) peaks for (a) O K-edge and (b) Ru L_3-edge XAS, where the fitted peaks and raw spectra are shown in Figure S2 and S3.

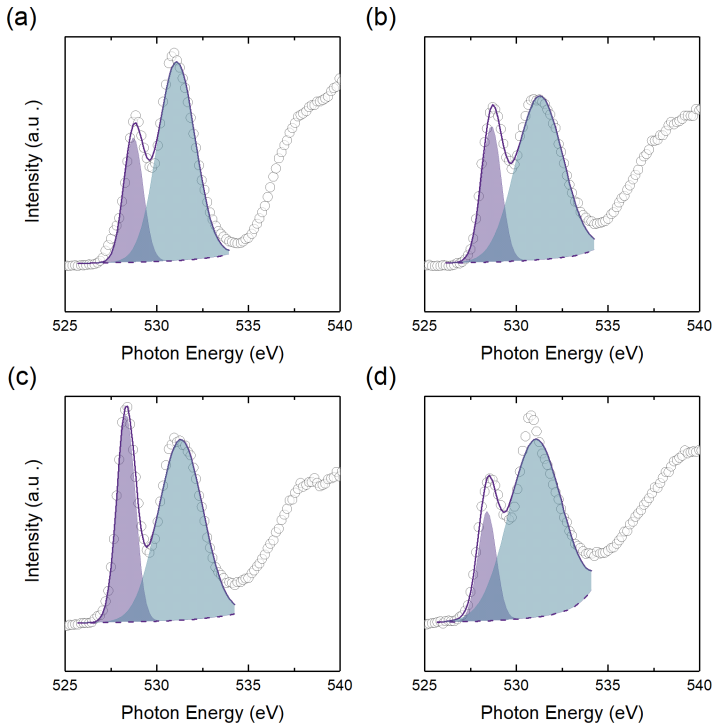

Figure S2: Fitted spectra (shaded area and line) and raw spectra (open circle) of O K-edge XAS of $Li_{2-x}RuO_3$ (a) pristine, and charged to (b) 3.6 V_{Li} (c) 3.8 V_{Li} and (d) 4.6 V_{Li}. Note that for consistency, we only fit two peaks of Gaussian shape with an arctangent background (dashed line) for all the spectra. Due to the broadening of the e_g peak, the fitting results at higher voltages is less ideal compared to fitting for the other voltages. The error of the fitting is estimated through fitting residuals and X^2 distribution ($X^2 = \sum_{i=1}^{n}(\frac{(y_i - f(x_i))^2}{\sigma_i^2})$). To reduce the variability of the fit, the arctangent background is constrained to have a height and width of 1 eV, with center around 536 eV for all the spectra obtained by pre-fitting with the background up to 560 eV and then fixed when fitting the pre-peak.

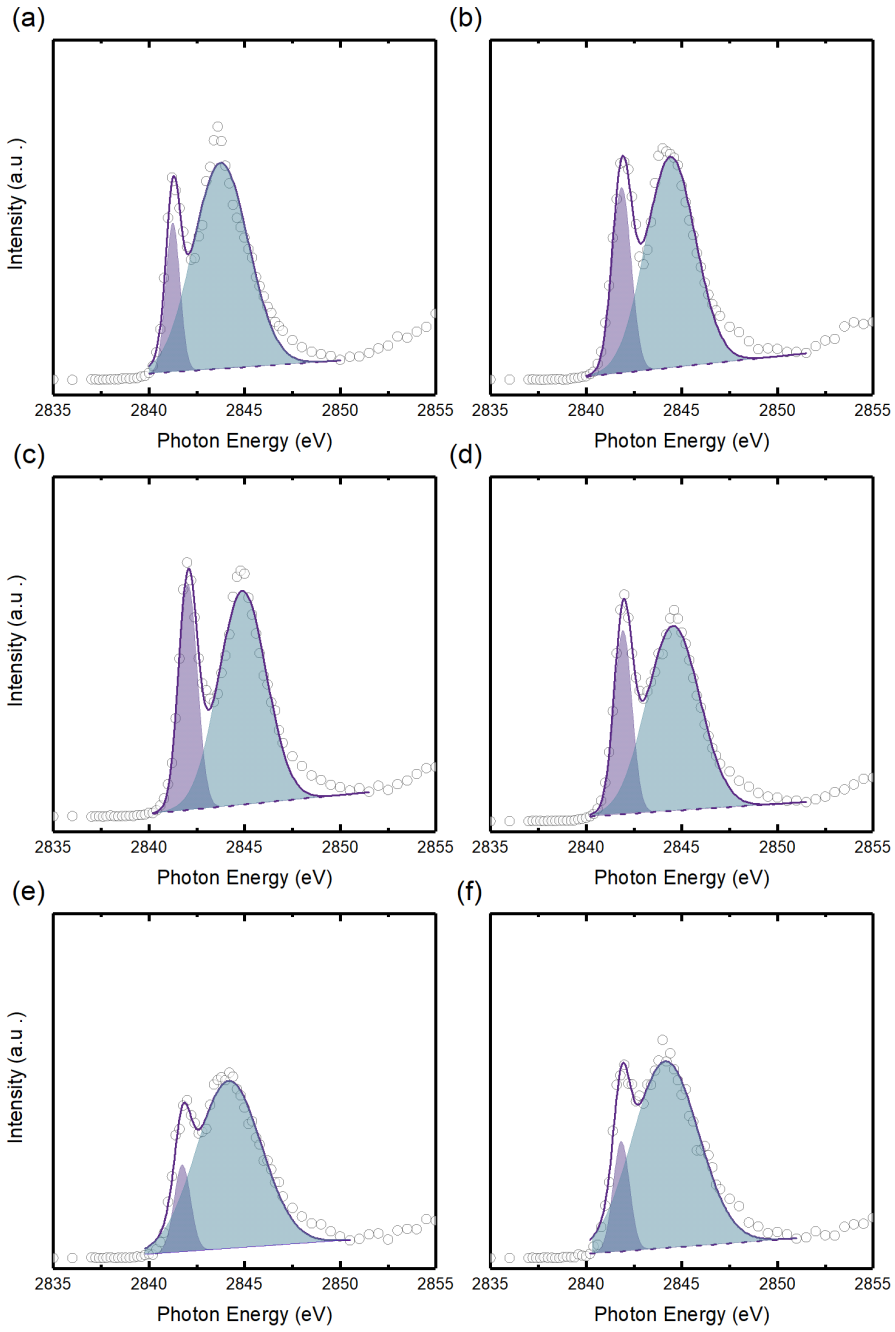

Figure S3: Fitted spectra (shaded area and line) and raw spectra (open circle) of Ru L_3-edge XAS of $Li_{2-x}RuO_3$ (a) pristine and charged to (b) 3.6 V_{Li} (c) 3.8 V_{Li}, (d) 4.2 V_{Li}, (e) 4.4 V_{Li} and (f) 4.6 V_{Li}. Note that for consistency and the absence of obvious background, we only fit two peaks of Gaussian shape with a linear background (dashed line) for all the spectra, and due to the broadening of the e_g peak, the fitting results at higher voltages are less ideal compared to fitting for the other voltages, and the error of the fitting is estimated through fitting residuals and X^2 distribution ($X^2 = \sum_{i=1}^{n}(\frac{(y_i - f(x_i))^2}{\sigma_i^2})$)

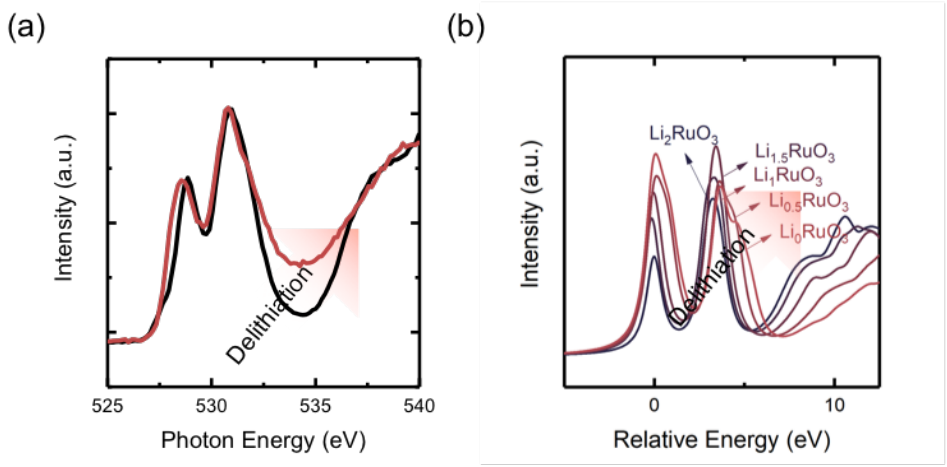

Figure S4: Experimental O K-edge XAS of pristine and charged $Li_{2-x}RuO_3$ to 4.6 V_{Li} (left) compared with computed O K-edge spectra of $Li_{2-x}RuO_3$ (right), where we observed a shoulder peak growing at higher photon energy for both the experimental and computed spectra. However, we should note that the relative intensity of the t_{2g} and e_g peaks in the computed O K-edge spectra is much higher than the experimental observed peak ratio for fully delithaited $Li_{2-x}RuO_3$

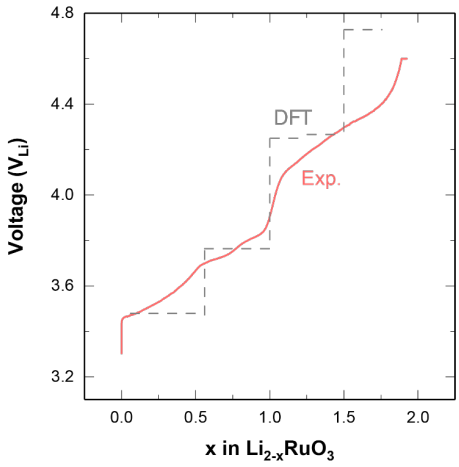

Figure S5: Calculated charge profile (by computing the energetics of the following delithiation reaction $Li_{2-x}RuO_3 = Li_{2-x-y}RuO_3+yLi$) (grey dashed line) of delithiated $Li_{2-x}RuO_3$ structures compared to experimental charging profile (red solid line), where the DFT calculated profile matched with the experimental profile and the most stable structure calculated from each step is used for spectra simulation in Figure 2 and Figure S4.

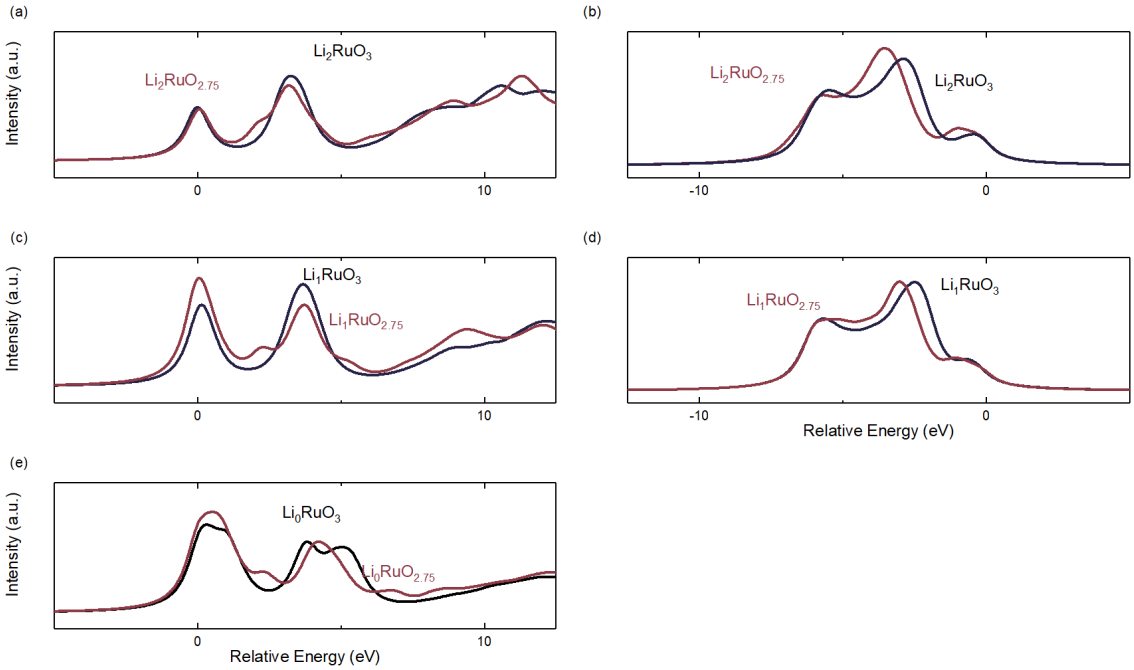

Figure S6: Simulated O K-edge XAS spectra of $Li_{2-x}RuO_3$(black) and defective $Li_{2-x}RuO_{3-\delta}$(red) structures ($\delta = 0.25$) for (a) x = 0 (c) x = 1, and (e) x = 2, and simulated O K-edge XES spectra of defective $Li_{2-x}RuO_{3-\delta}$ structures ($\delta = 0.25$) for (b) x = 0 and (d) x = 1. Similarly as in Ru L_3-edge (Figure S7), we can note that as we introduce oxygen vacancies in the structure, in the O K-edge XAS, the e_g peak intensity decreased, while creating additional feature between the t_{2g} and e_g features at all lithium contents. In the simulated O K-edge XES, as we introduce oxygen vacancies, we only observed the shift of the non-bonding peak towards lower photon energy without creation of additional peak. Therefore, introduction of oxygen vacancies cannot explain the broadening we observed in the experimental XES data.

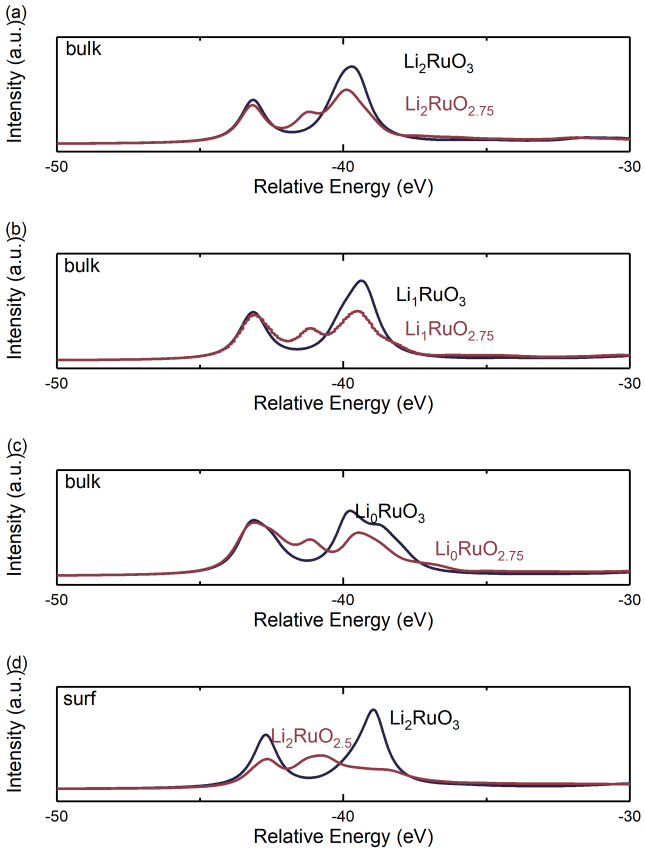

Figure S7: Simulated Ru L_3-edge XAS spectra of $Li_{2-x}RuO_3$(black) and defective $Li_{2-x}RuO_{3-\delta}$ structures ($\delta = 0.25$) for (a) x = 0 (b) x = 1, and (c) x = 2, and (d) the simulated Ru L_3-edge XAS spectra of surface Ru atom with O vacancy concentrated on the surface is also included. We note that as we introduce oxygen vacancies in the structure, the e_g peak intensity decreased, while creating additional feature between the t_{2g} and e_g features at all lithium contents.

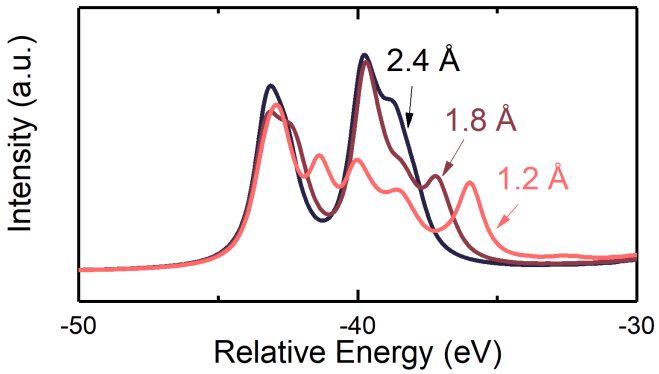

Figure S8: Simulated Ru L-edge XAS spectra of Li_0RuO_3 structure with oxygen-oxygen bond length of around 2.4 Å and hypothetical structures by forcing oxygen and oxygen bond length to 1.8 Å and 1.2 Å. We can note that as we introduce shorter oxygen-oxygen bond, the additional

shoulder we observed at high photon energy representing O-O σ* feature shifted to higher energy, which indicates that as two oxygen atoms are forces closer together the (O-O) σ* feature is destabilized. Moreover, by modulating the O-O bond length from 1.8 Å to 1.2 Å, the e_g peak reduces in area compared to t_{2g} feature, which is not observed at high potentials in the experimental spectra in Figure 1(b) and 2(a), therefore in $Li_{2-x}RuO_3$ system, the creation of superoxo-species (with O-O bond distance less than 1.5 Å) is not likely or not stable to be observed.

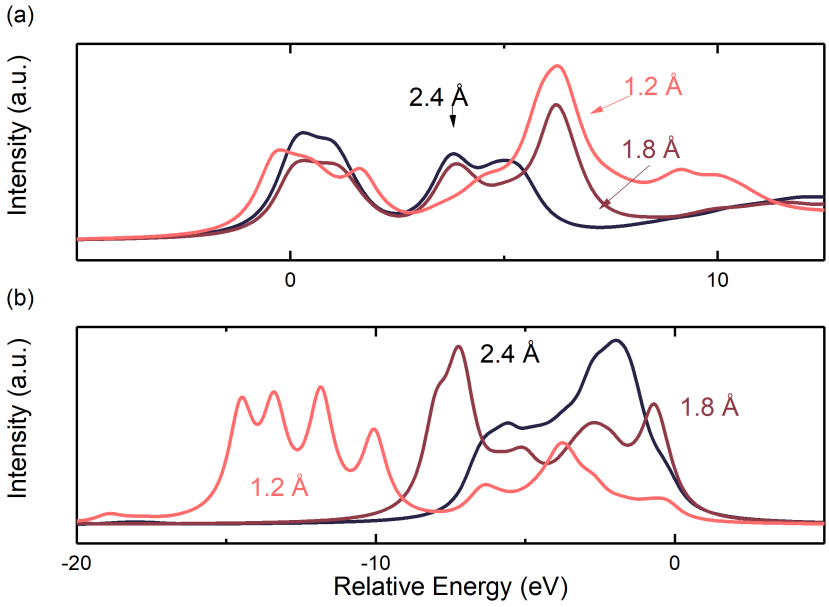

Figure S9: Simulated O K-edge (a) XAS and (b) XES spectra of Li_0RuO_3 structure with oxygen-oxygen bond length of around 2.4 Å and hypothetical structures obtained by forcing the oxygen and oxygen bond length to 1.8 Å and 1.2 Å. For XAS, we note that as we shorten the oxygen-oxygen bond, the additional shoulder we observed at high photon energy representing O-O σ* feature shifts to higher energy and increases in intensity (see also the Ru L-edge simulation as shown in Figure S8.) This indicates that as the two oxygens are forced to be closer together, the σ* feature is destabilized. Moreover, by modulating the O-O bond length from 1.8 Å to 1.2 Å, the e_g peak drastically reduces in area compared to t_{2g} feature, which is not observed at high potentials in the experimental spectra in Figure 1(a) and 2(a). Compared to the XAS spectra, the computed XES spectra is more sensitive to the fluctuation of oxygen bond distance. Upon decreasing the bond distance, there are more features observed in the XES spectra, potentially coming from the clear fingerprint of $\sigma, \pi, \pi*$ feature of the O-O bond due to stronger oxygen coupling. This splitting is not observed in the experimental spectra either. Therefore in $Li_{2-x}RuO_3$ system, the creation of superoxo- and peroxo-species (with O-O bond distance less than 1.5 Å) is not likely or not stable enough to be observed.

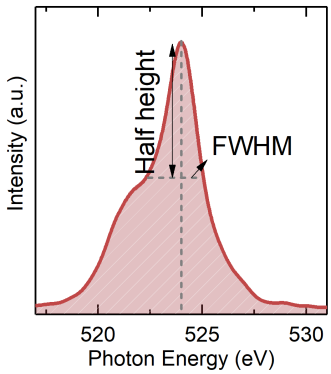

Figure S10 Schematics of an example FWHM extraction of O K-edge XES spectra. The FWHM was estimated through the width of the center peak at half height since the center non-bonding peak is much taller than the shoulder peaks, therefore we assume the shoulder peaks evolution will not have significant effect on the full width half maximum of the center non-bonding peak.

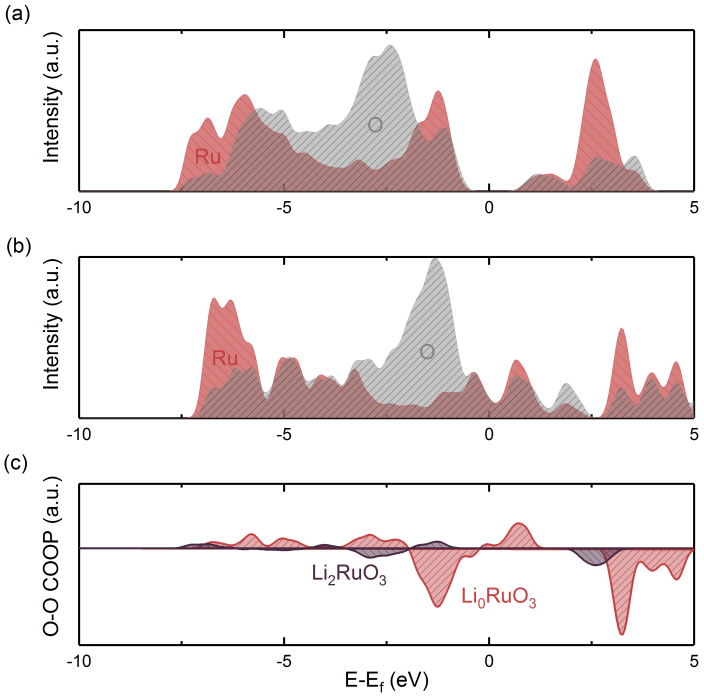

Figure S11: Calculated ground-state pDOS of (a)Li_2RuO_3 and (b)Li_0RuO_3 used for the calculation of crystal orbital overlap population (COOP) in (c), where as we delithiated the Li_2RuO_3, there is a significant increase of O-O coupling, which can be observed in experimental Ru L_3-edge and O K-edge XAS as well as O K-edge XES.

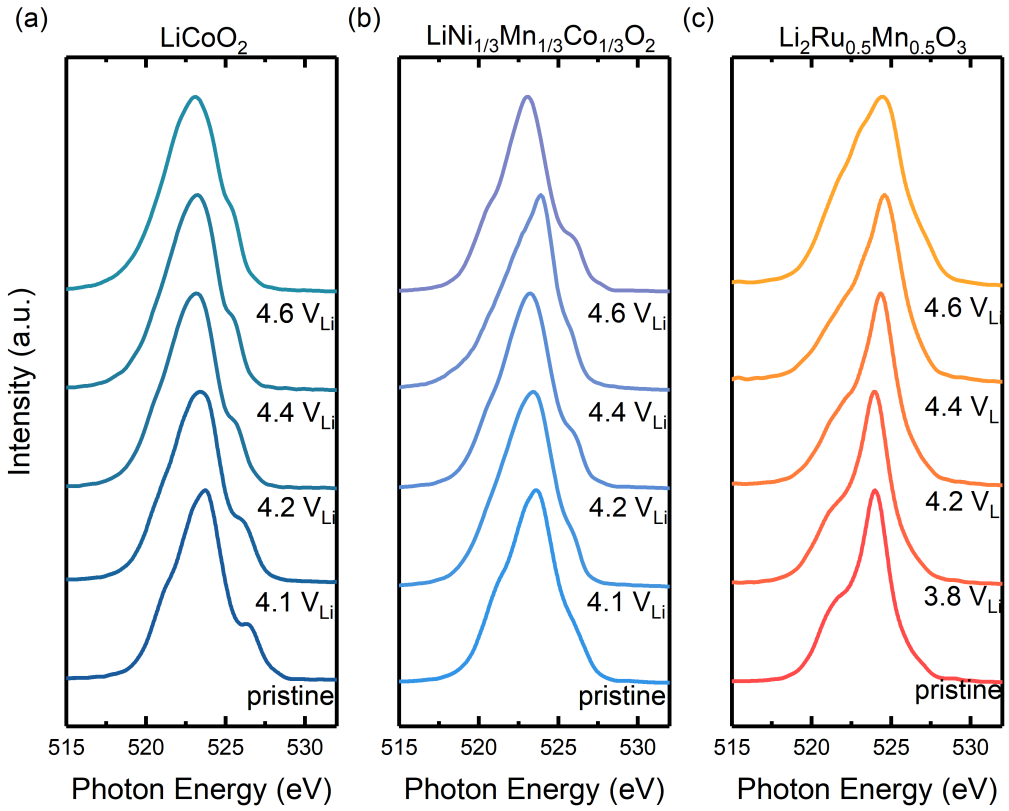

Figure S12 Experimental O K-edge XES of (a) pristine and charged $Li_{1-x}CoO_2$ to 4.1 V_{Li}, 4.2 V_{Li}, 4.4 V_{Li}, and 4.6 V_{Li}, (b) pristine and charged $Li_{1-x}Ni_{1/3}Mn_{1/3}Co_{1/3}O_2$ to 4.1 V_{Li}, 4.2 V_{Li}, 4.4 V_{Li}, and 4.6 V_{Li}, and (c) pristine and charged $Li_{2-x}Mn_{0.5}Ru_{0.5}O_3$ to 3.8 V_{Li}, 4.2 V_{Li}, 4.4 V_{Li}, and 4.6 V_{Li}, where, upon delithiation, materials exhibiting anionic redox including $Li_{2-x}Ru_{0.5}Mn_{0.5}O_3$ and $Li_{2-x}RuO_3$ showed significant broadening of non-bonding peak, in contrast with $Li_{1-x}CoO_2$ and $Li_{1-x}Ni_{1/3}Mn_{1/3}Co_{1/3}O_2$ which relied primarily on cationic redox and did not show significant changes, as shown in Figure 3(e) and Figure S13.

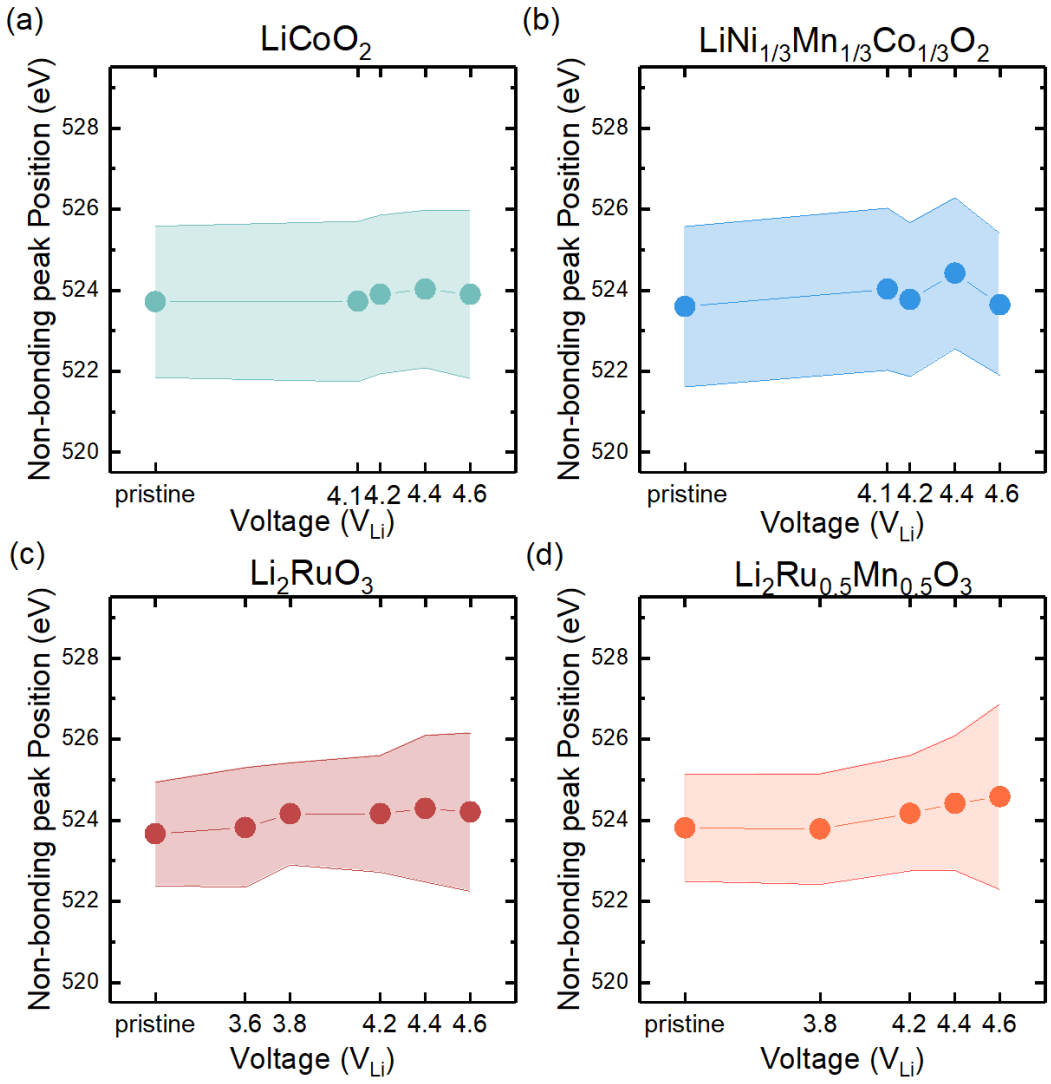

Figure S13: Non-bonding peak position (closed circle) and FWHM (colored band) of O K-edge XES of (a) pristine and charged $Li_{1-x}CoO_2$ to 4.1 V_{Li}, 4.2 V_{Li}, 4.4 V_{Li}, 4.6 V_{Li} , (b) pristine and charged $Li_{1-x}Ni_{1/3}Mn_{1/3}Co_{1/3}O_2$ to 4.1 V_{Li}, 4.2 V_{Li}, 4.4 V_{Li}, 4.6 V_{Li} , (c) pristine and charged $Li_{2-x}RuO_3$ to 3.6 V_{Li}, 3.8 V_{Li}, 4.2 V_{Li}, 4.4 V_{Li}, 4.6 V_{Li} and (d) pristine and charged Li_{2-} $Ru_{0.5}Mn_{0.5}O_3$ to 3.8 V_{Li}, 4.2 V_{Li}, 4.4 V_{Li}, 4.6 V_{Li} , where, upon delithiation, materials exhibiting anionic redox including $Li_{2-x}Ru_{0.5}Mn_{0.5}O_3$ and $Li_{2-x}RuO_3$ showed significant broadening of non-bonding peak, in contrast with $Li_{1-x}CoO_2$ and $Li_{1-x}Ni_{1/3}Mn_{1/3}Co_{1/3}O_2$ which relied primarily on cationic redox and did not show significant changes, as shown in Figure 3(e). Here, the FWHM was extracted based on the width at the half height of the most predominant peak (non-bonding peak) as the other shoulder peaks are much smaller than non-bonding peak, thus we assume that the shoulder peaks evolution will not have significant effect on the FWHM of the center non-bonding peak, the FWHM extraction procedure is also shown schematically in Figure S10.

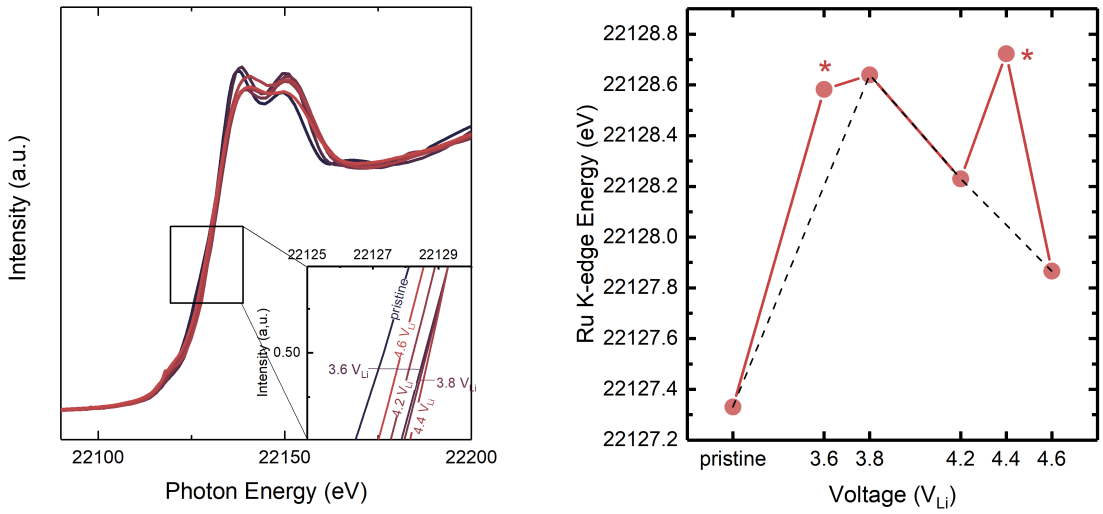

Figure S14: Ru K-edge XAS spectra (left) of pristine $Li_{2-x}RuO_3$, and charged to 3.6 V_{Li}, 3.8 V_{Li}, 4.2 V_{Li}, 4.4 V_{Li} and 4.6 V_{Li}, where the quantification of the K-edge energy is shown on the right. Here we can see that Ru K-edge shifted towards higher photon energy up to 3.8 V_{Li} by removing around 1 lithium per formula unit, representing $Ru^{4+/5+}$ oxidation, and upon further lithium de-intercalation the edge shifted toward lower photon energy as we charge up to 4.6 V_{Li} creating small shoulder in the pre-peak region around 22125 eV, signalizing Ru reduction and Ru-O cage distortion. This observation matches with what we have observed in Figure 1 and Figure 2 in O K-edge, Ru L_3-edge data and K-edge X-ray near edge absorption spectroscopy (XANES) data. All the data were aligned with a Ru metal foil reference channel. We should note that the data for $Li_{2-x}RuO_3$ charged to 3.6 V_{Li} and 4.4 V_{Li} (marked asterisk) were measured at a different beamtime, and had a slightly higher edge energy compared to the dashed line trend built by the other data even after reference channel alignment.

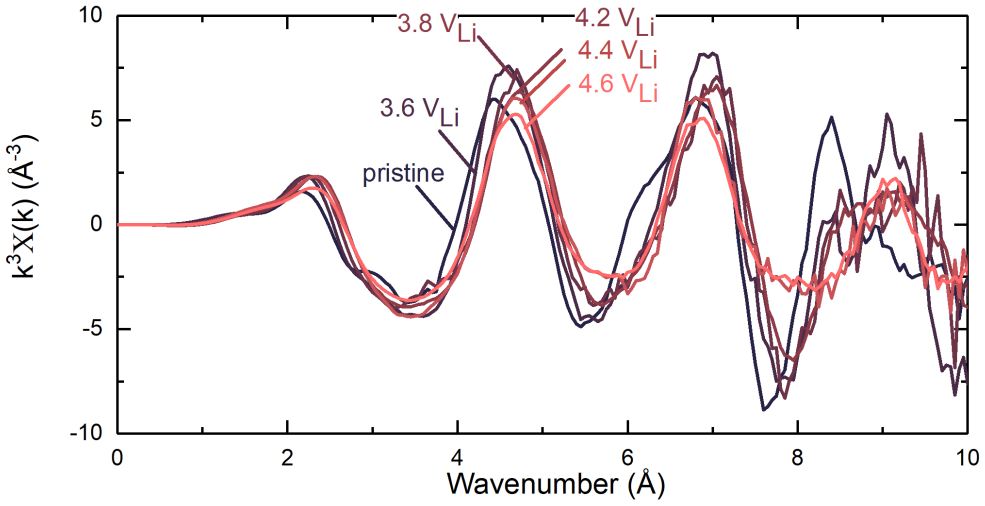

Figure S15: Ru K-edge EXAFS spectra in k-space of pristine $Li_{2-x}RuO_3$, and charged to 3.6 V_{Li} 3.8 V_{Li}, 4.2 V_{Li}, 4.4 V_{Li} and 4.6 V_{Li}. The signal becomes rather noisy after 8 Å, and a confident fitting for the second and third coordination shell is challenging.

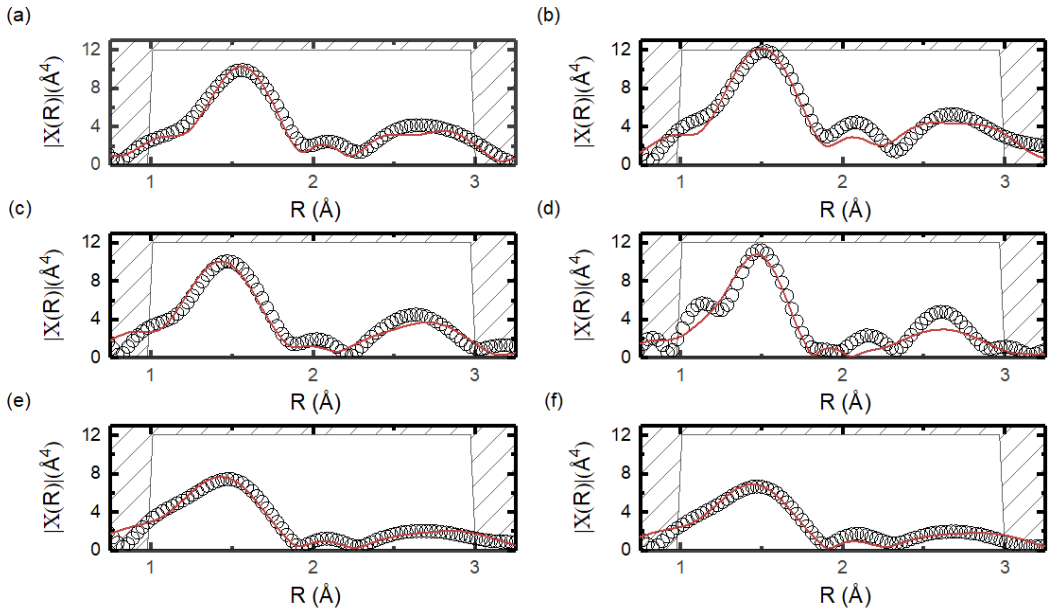

Figure S16: Fitted Ru K-edge EXAFS spectra in R-space of (a) pristine $Li_{2-x}RuO_3$, and charged to 3.6 V_{Li} (c) 3.8 V_{Li}, (d) 4.2 V_{Li}, (e) 4.4 V_{Li} and (f) 4.6 V_{Li}, where we note that the fit for (d) 4.2 V_{Li} is very challenging.

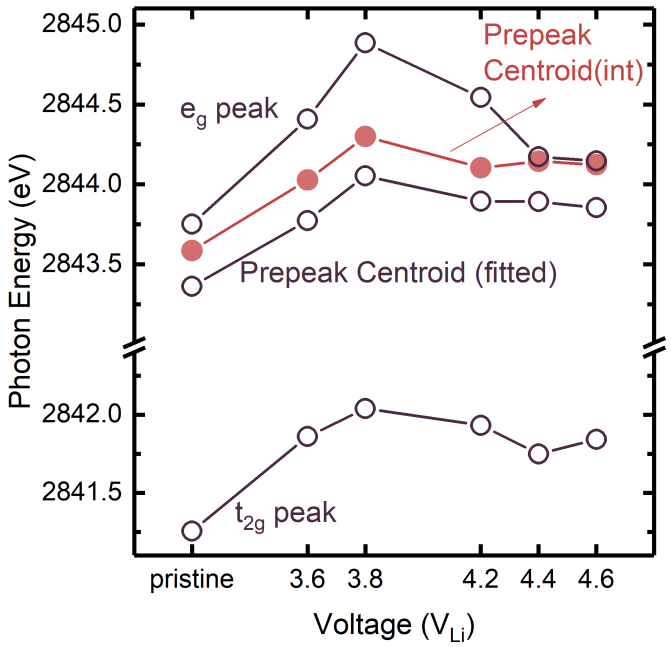

Figure S17: The t_{2g} and e_g peak (white-line) position, pre-peak centroid calculated through the fitting in Figure S3 as well as through simple integration of the area above the linear fitted background in Figure S3 of pristine $Li_{2-x}RuO_3$, and charged to 3.6 V_{Li}, 3.8 V_{Li}, 4.2 V_{Li}, 4.4 V_{Li} and 4.6 V_{Li}. Regardless of method used to process the Ru L_3-edge spectra to obtain the oxidation state of Ru, it always shows a monotonic oxidation up to 3.8 V_{Li} and a slight reduction of Ru charging to 4.2 V_{Li} and above. We should also note that the pre-peak centroid positions calculated from fitting are always slightly lower than that computed from simple integration method because the fitting of e_g peaks do have more residuals compared to the fitting of t_{2g} peak, especially at high potentials, due to creation of high-photon energy features. To maintain consistency of fitting, we always fit only two peaks for the major two features observed in the raw spectra.

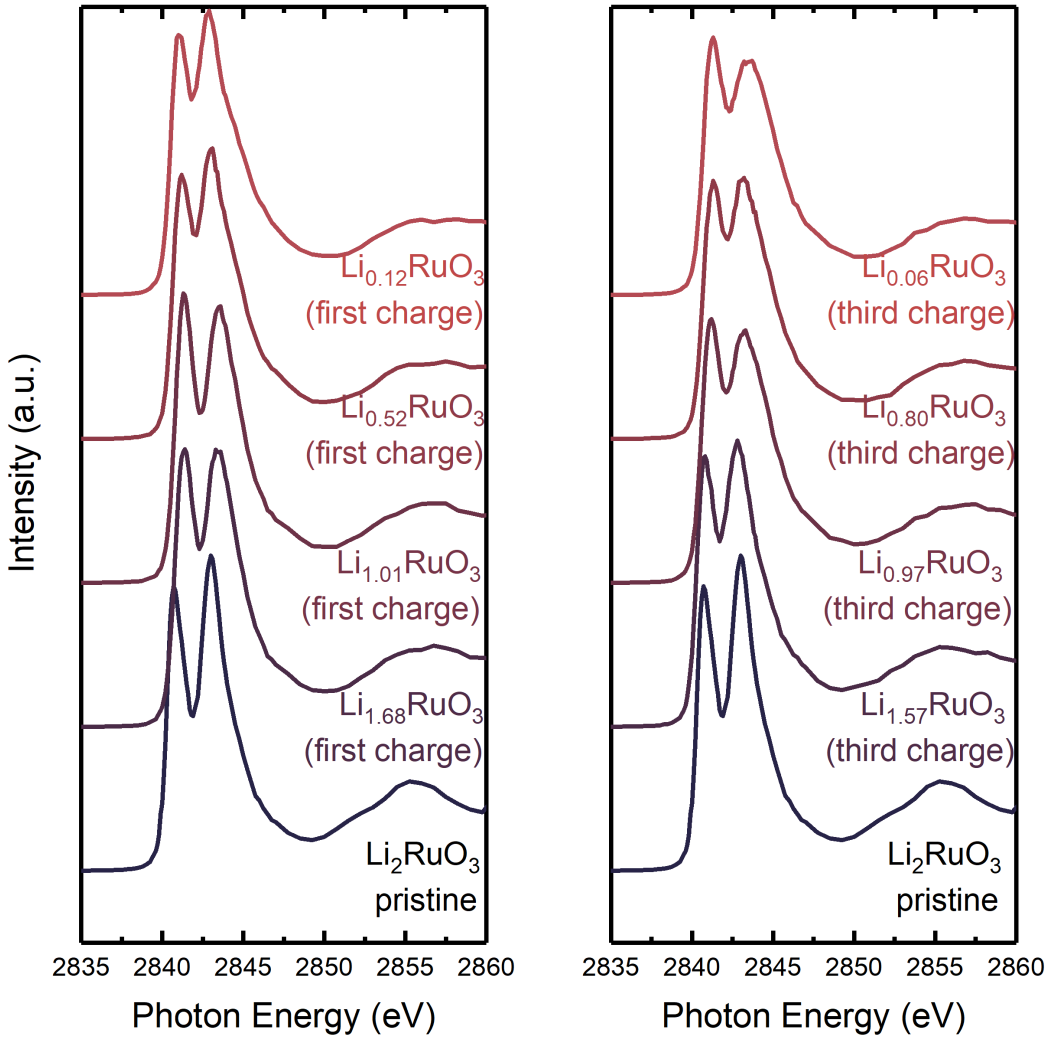

Figure S18: Ru L_3-edge XAS of charged $Li_{2-x}RuO_3$ composite electrodes in the first and third cycle. Despite a similar state of charge in the first and third cycle, Ru started in a much more reduced state in the third cycle, shown also in Figure 5. We note that this composite electrode is much more concentrated than the pellet we prepared for the oxide-only pellets shown in Figure 1. Therefore, in fluorescence mode there is a large self-absorption effect in the composite samples. The change in the peak shape is overwhelmed by the self-absorption effect and cannot be compared directly to the oxide-only result.

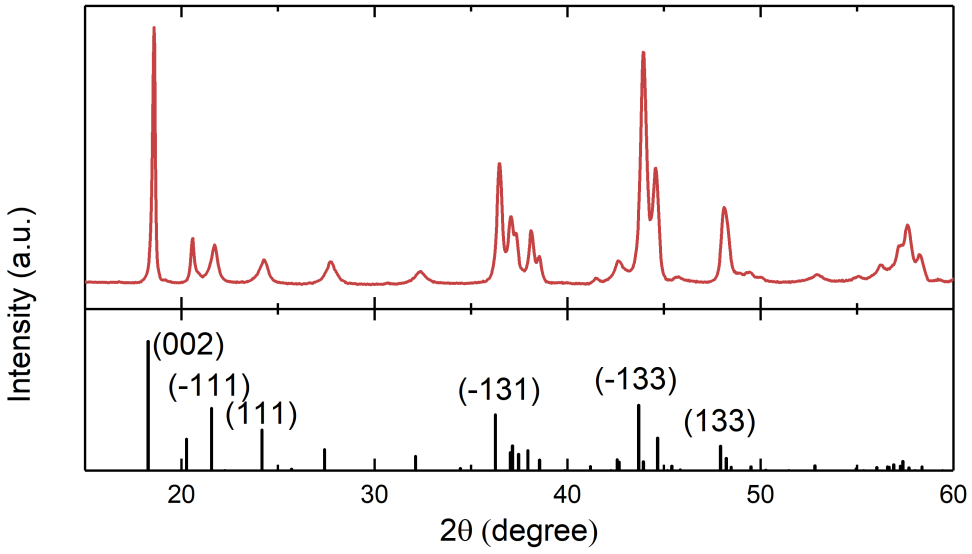

Figure S19: Powder X-ray diffraction (XRD) of the synthesized Li_2RuO_3, where there are no impurity peaks observed. The reference XRD is shown in lower panel with respective Miller indices labeled for major peaks (Ref. 77)

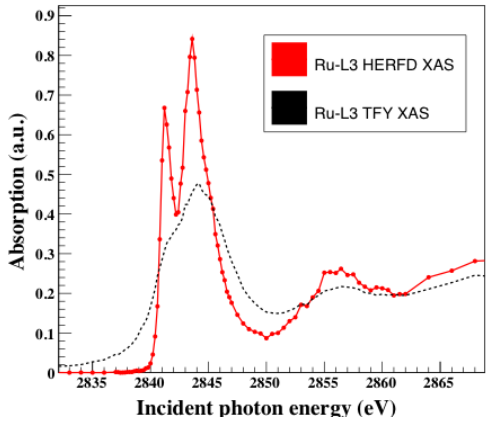

Figure S20: A comparison between conventional total fluorescence yield (TFY) and HERFD X-ray absorption of Ru L_3-edge as measured in pristine Li_2RuO_3.

Table S1: Detailed fitting parameter for the EXAFS fitting of the first coordination shell where the coordination number, amplification reduction factor (S_0^2), bond length (R_{Ru-O}), energy shift (E_0)as well as the pseudo Debye-Waller factor σ^2_{Ru-O}, and their associated standard deviation (std) obtained from fitting are reported. The R window we have included 1 to 3 Å and we have also included the second coordination shell (Ru-Ru) in the fitting.

Voltage	**N**	**S_0^2**	**std (S_0^2)**	**R_{Ru-O}**	**std(R_{Ru-O})**	**E_0**	**Std(E_0)**	**σ^2_{Ru-O}**	**Std(σ^2_{Ru-O})**
Pristine	6	0.831	0.173	2.028	0.021	0.816	3.041	0.0035	0.0028
3.6 V_{Li}	6	0.951	0.219	1.980	0.023	-1.753	3.481	0.0030	0.0030
3.8 V_{Li}	6	0.877	0.214	1.941	0.021	-5.884	3.697	0.0039	0.0029
4.2 V_{Li}	6	0.850	0.102	1.941	0.011	-4.516	1.738	0.0044	0.0015
4.4 V_{Li}	6	1.125	0.122	1.958	0.011	-3.512	1.552	0.0093	0.0016
4.6 V_{Li}	6	0.910	0.112	1.964	0.013	-3.649	1.828	0.0080	0.0018

Table S2: Detailed fitting parameter for the EXAFS fitting of the first coordination shell where the coordination number, amplification reduction factor (S_0^2), bond length (R_{Ru-O}), energy shift (E_0)as well as the pseudo Debye-Waller factor σ^2_{Ru-O}, and their associated standard deviation (std) obtained from fitting are reported. The R window we have included 1 to 2.3 Å and we did not include the second coordination shell (Ru-Ru) in the fitting. We should note that the trend we observed for the Debye-Waller factor and the Ru-O bond length still holds even if we only include the first coordination shell.

Voltage	**N**	**S_0^2**	**std (S_0^2)**	**R_{Ru-O}**	**std(R_{Ru-O})**	**E_0**	**Std(E_0)**	**σ^2_{Ru-O}**	**Std(σ^2_{Ru-O})**
Pristine	6	0.838	0.107	2.028	0.013	0.394	1.789	0.0035	0.0016
3.6 V_{Li}	6	0.923	0.144	1.981	0.015	-1.579	2.209	0.0026	0.0020
3.8 V_{Li}	6	0.761	0.095	1.952	0.012	-3.895	1.831	0.0028	0.0015
4.2 V_{Li}	6	0.809	0.080	1.948	0.010	-3.363	1.510	0.0041	0.0013
4.4 V_{Li}	6	0.971	0.152	1.956	0.016	-3.222	2.158	0.0077	0.0024
4.6 V_{Li}	6	0.805	0.108	1.964	0.014	-3.158	1.883	0.0068	0.0020